

The effect of binder thickness and residual stresses on the fracture toughness of cemented carbides

RAYMOND A. CUTLER*

Terra Tek, Inc, 400 Wakara Way, Salt Lake City, Utah 84108, USA

ANIL V. VIRKAR

Department of Materials Science and Engineering, University of Utah, Salt Lake City, Utah 84112, USA

Much of the data on WC-Co cermets show that the fracture toughness, K_{Ic} , increases with increasing tungsten carbide grain size at fixed volume fraction of the cobalt binder phase. It is shown that the origin of this effect can be explained on the basis of the plane stress fracture of constrained cobalt phase and the periodic internal stresses arising due to differential thermal contraction of the two phases. Quantitative models have been derived which take these two effects into account. The effect of macroscopic residual stresses, such as those generated by milling WC-Co drilling inserts, on the apparent toughness has also been analysed. It is shown that for the chevron-notched type specimen the macroscopic residual stress affects not only the maximum load but also the length of the crack at which the maximum occurs. A graphical method is presented which permits the evaluation of the true K_{Ic}^0 .

1. Introduction

WC-Co composites combine an abrasive ceramic (tungsten carbide) with a ductile metal (cobalt) by sintering the powder composite at temperatures above the melting point of the metallic phase. These ceramic-metal (cermet) composites are relatively hard and much tougher than ceramics, and are therefore used as drilling inserts, cutting tools and wear parts in applications where ceramics perform poorly. A considerable amount of work has been done to characterize fracture mechanical properties of WC-Co cements. Kenny [1], Yen [2] and Ingelstrom and Nordberg [3] showed that the fracture toughness increases with increasing cobalt content. Lueth [4, 5] found that the critical strain energy release rate (G_{Ic}) for WC-Co is linearly related to the binder film thickness. While Chermant and Osterstock [6] found a

similar linear relationship as Lueth, they showed that a better linear fit resulted when G_{Ic} was plotted against d_2^2/d_1 , where d_1 is the mean tungsten carbide grain size and d_2 is the mean binder film thickness. This parameter was obtained by equating the energy of a dislocation pile-up in the cobalt film with the energy necessary to break a carbide grain. They suggested that crack propagation in WC-Co occurs by the plastic flow of cobalt, which causes the fracture of carbide grains ahead of the crack. Later, the same authors proposed that two mechanisms were acting simultaneously: (1) sliding and interfacial decohesion of the carbide-carbide boundaries, and (2) deformation and tearing of the cobalt phase [7]. Murray [8] showed that fracture in WC-Co is governed by plastic flow at the crack tip and that the total crack tip plastic zone size is equal to the thickness of the highly con-

*Present address: Ceramatec, Inc, 163 West 1700 South, Salt Lake City, Utah 84115, USA.

strained binder. Pickens and Gurland [9] found that fracture occurred by interfacial decohesion in fine-grained alloys ($d_1 < 2 \mu\text{m}$) or by tungsten carbide cleavage in coarse-grained alloys ($d_1 > 2 \mu\text{m}$), followed by extensive plastic deformation and rupture of the binder ligaments. They showed that the relation

$$G_{1c} = \alpha\sigma_y d_2 \quad (1)$$

where σ_y is the yield strength of the binder and α is a constant, was applicable for fine-grained alloys and explained this based on the ductile-fracture criterion proposed by Rice and Johnson [10]. Viswanadham *et al.* [11] claimed that dislocations in the binder phase invalidate Murray's view that the binder deforms at its theoretical shear strength and suggested instead that the critical strain energy release rate can be described by

$$G_{1c} \simeq \alpha\sigma_y \varepsilon_f A_f^{\text{Co}} d_2 \quad (2)$$

where ε_f is the fracture strain, A_f^{Co} is the area fraction of cobalt on the fracture surface and d_2 is the mean free path of cobalt taking the contiguity of the carbide into account. The strain energy release rate was therefore equal to the volume of deformed binder per unit area of the fracture surface ($A_f^{\text{Co}} d_2$) times the plastic work performed per unit volume of deformed binder ($\simeq \sigma_y \varepsilon_f$). They noted a strictly linear relationship between G_{1c} and $(\sigma_y A_f^{\text{Co}} d_2)$ and concluded that the area fraction of binder, the mean free path and *in situ* yield behaviour of the binder are the three principal factors that determine the fracture toughness of cemented carbides. It is interesting to note, however, that $A_f^{\text{Co}} = V_v$ where V_v is the volume fraction of Co. V_v in turn is given by $V_v = S_v d_2 = 3d_2/d_1$ (3)

where S_v is the grain boundary area per unit volume ($= 3/d_1$ assuming spherical grains) and $V_v \ll 1$. Thus, Equation 2 can be rewritten as

$$G_{1c} = 3\alpha\sigma_y \varepsilon_f (d_2^2/d_1) \quad (4)$$

which is similar to the one proposed by Chermant and Osterstock [6]. This was confirmed by plotting the data of Viswanadham *et al.* [11] against d_2^2/d_1 , which exhibited a straight-line behaviour. Thus, the same data can be used to explain intergranular fracture through the binder or a fracture path dominated by contiguous WC-WC fracture. Furthermore, their

models predict that G_{1c} will be negligible if $V_v = 0$, contrary to observation.

Almond [12], in reviewing existing fracture toughness models, notes that none of the models have taken into account the work hardening rate of the binder and all of the models are still too empirical to be used in quantitatively predicting how fracture toughness could be improved without affecting other microstructurally dependent properties. The observed fact that fracture toughness increases more rapidly with increasing tungsten carbide grain size (at a constant volume per cent cobalt) for a high cobalt composition than for a low cobalt composition [6] has not been adequately explained. Nor do existing models explain why the fracture path changes from intergranular to transgranular as the tungsten carbide grain size increases.

Another important consideration with reference to WC-Co cermets is the role of thermal mismatch stresses on fracture. Rice [13] was the first to take the thermal mismatch stresses caused by differences in thermal expansion between the carbide and metal phases into account. His calculations suggest that the microscopic residual stresses in combination with the applied stress cause microcracking between carbide grains as well as plastic flow of the binder phase. The present paper presents an alternative explanation for the effect of microscopic residual stresses on fracture toughness by evaluating the stress intensity factor due to periodic internal stresses.

While it is widely recognized that macroscopic residual stresses induced by precompression [14], grinding [15, 16] and rapid cooling [17] affect mechanical properties, Barker [18] was the first to recognize that these stresses influence the apparent toughness when measured in the bulk and must be corrected for if a material property is to be obtained. This paper presents a quantitative method for evaluating the effect of macroscopic residual stresses on fracture toughness.

While it is understood that fracture in cemented carbides is complex and such fundamental questions as the mode of fracture in cemented carbides and the existence of thin cobalt films between apparently contiguous WC grains are still not resolved, this paper elucidates three important aspects of the fracture of cemented carbides: (1) the dependence of

fracture toughness on binder film thickness, (2) the effect of microscopic residual stresses on fracture toughness, and (3) the effect of macroscopic residual stress on apparent fracture toughness.

2. Analysis of fracture toughness

2.1. Binder film thickness effects

The thickness of the cobalt binder (the mean free path of the binder) ranges between 0.1 and 1.0 μm in commercial grades of cemented carbides. During fracture, the thin filaments of the ductile metal must be ruptured. The cobalt binder is highly constrained by the tungsten carbide grains. Thus, one must examine the fracture of constrained films. Early experiments by Irwin *et al.* [19] showed that the critical strain energy release rate is dependent on the specimen thickness for thin plates. For a 7075-T6 alloy the value of G_C increased linearly up to a thickness of 2 mm and then decreased, reaching a constant value above 15 mm [19, 20] beyond which plane strain conditions prevailed. In thin sheets the state of stress is essentially that of plane stress and crack extension occurs by an antiplane strain (K_{III}) mechanism even though the loading is tensile. Failure of unconstrained cobalt ligaments must occur in plane stress. One would therefore expect that the toughness of cobalt itself will increase with increasing thickness. In order to see if G_C increases linearly for cobalt in the 0.1 to 1.0 μm range, it is necessary to test cobalt foils to failure. Since such foils were not available, thin sheets of nickel[†] were tested in tension. Thin sheets of two thicknesses, namely 5 and 13 μm , and of width 2.5 cm, with a central crack of length 1.0 cm, were tested to failure in tension in a universal testing machine[‡] at 0.25 mm min⁻¹. The critical stress intensity factor (K_C) was determined using the following relationship derived by Irwin [19]:

$$K = \sigma[w \tan(\pi a/w)]^{1/2} \quad (5)$$

where σ is the applied stress, w is the total width of the specimen, and a is one-half the crack length. A total of seven 13 μm thick specimens were tested with a mean K_C of 23.7 MPa m^{1/2} (standard deviation of 3.1), while the six 5 μm thick foils resulted in a mean K_C of 14.7 MPa m^{1/2} (standard deviation of 3.5). Using a value of 207 GPa for the Young's modulus of nickel and

0.3 for Poisson's ratio, mean G_C values of 2471 J m⁻² and 950.7 J m⁻² were calculated for the 13 and 5 μm foils, respectively. Using a value of 0 J m⁻² for zero thickness, a perfect linear relationship results when G_C is plotted against thickness. The K_C of pure unrestrained nickel of thickness 0.1 μm and 1.0 μm is calculated to be 2.1 MPa m^{1/2} and 6.6 MPa m^{1/2} respectively based on this linear fit. SEM micrographs showed that the foils had fractured on a 45° angle relative to the tensile axis, typical of an unconstrained foil failing in the K_{III} mode. It is not clear that this K_{III} mode can occur if the foil is constrained to prevent buckling. Results by Irwin *et al.* [19], however, showed that the toughness of 800 μm thick plates increased by a factor of 2 when buckling was restrained. This suggests that the fracture toughness of the highly constrained cobalt binder is the major contribution to the fracture toughness of cemented carbides. The primary reason for the linear increase in G_C with increasing mean free path of cobalt is the linearly increasing fracture toughness of the cobalt binder.

When the fracture of thin sheets occurs in the K_{III} mode, it has been shown [20] that

$$G_C = \frac{2\sqrt{2} \sigma_y B}{(1 + \nu)} \approx 2\sigma_y B \quad (6)$$

where B is thickness of the sheet. Replacing B by d_2 , the mean free path of cobalt, and assuming spherical WC grains of diameter d_1 , results in the following relationship:

$$d_2 = (d_1 V_v)/3 \quad (7)$$

where V_v is the volume fraction of cobalt (we assume $V_v \ll 1$). Equating d_2 in Equations 6 and 7 gives

$$G_C = (2\sigma_y V_v d_1)/3 \quad (8)$$

for the critical strain energy release rate of the binder. Using the subscripts 1 and 2 to denote the carbide and cobalt phases respectively, the total strain energy release rate can be written as:

$$G = G_{(1)}(1 - V_v) + (2\sigma_y V_v^2 d_1)/3 \quad (9)$$

(Note that as $V_v = 3d_2/d_1$, the above relationship also yields $G = G_{(1)}(1 - V_v) + 6\sigma_y d_2^2/d_1$ similar to Chermant and Osterstock [6].) Using

[†]WEP electroformed nickel foil, 99.95% pure, Wiggin Electrochemical Products, Birmingham, UK.

[‡]Model 1125, Intron Corp, Canton, MA, USA.

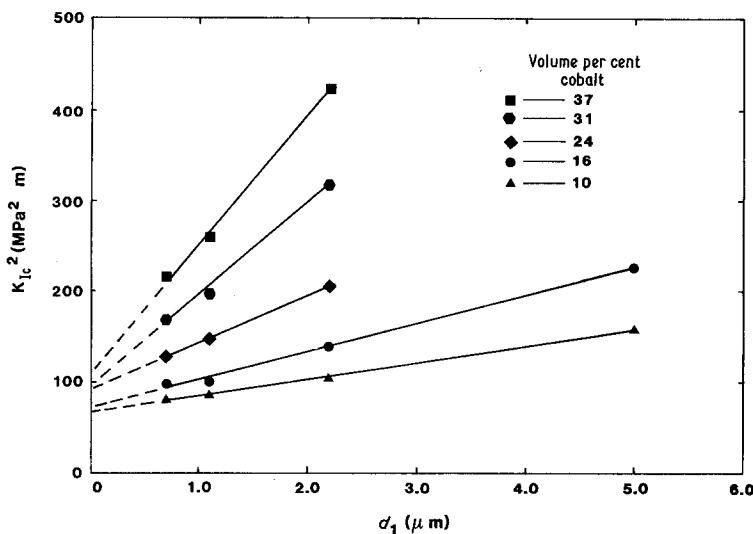


Figure 1 Experimental data of Chermant and Osterstock [6, 7] showing linear fit which results when K_{Ic}^2 is plotted against d_1 for a constant volume per cent cobalt.

the relationship

$$K_{Ic}^2 = G_{Ic}E(1 - \nu^2) \quad (10)$$

and neglecting the contribution due to Poisson's ratio (ν) gives the following approximation for the fracture toughness of cemented carbides:

$$K_{Ic}^2 = G_{Ic(l)}(1 - V_v)E + (2\sigma_y EV_v^2 d_1)/3 \quad (11)$$

If this relationship is valid, a plot of critical stress intensity squared versus mean WC grain size should be linear with slope $2\sigma_y EV_v^2/3$ and intercept $G_{Ic(l)}(1 - V_v)E$. Plotting the data of Chermant and Osterstock [6, 7] in Fig. 1 shows that a linear fit with a correlation coefficient greater than 0.99 results for each cobalt level (see Table I). Not only does this verify the linear increase in G_C with increasing cobalt thickness suggested by the toughness tests on the nickel sheets, it also allows an estimate of the yield strength of the constrained binder to be made from the slope of Fig. 1 (see Table I). Since Equation 11 assumes spherical WC grains, the slope was multiplied by $(1 - C)$, where C is the fraction of contiguous WC grains [7]. The mean yield strength of 1483 MPa is considerably

higher than earlier estimates [11, 21]. However, it has been shown [22] that a cast Co-20WC alloy (the 20 wt % WC is primarily dissolved in the cobalt phase) exhibits a yield stress of nearly 800 MPa in a bulk sample. Commercial WC-Co grades also have substantial amounts of tungsten dissolved in the cobalt binder. The cobalt ligaments are very thin and constrained by the WC grains as opposed to the large cobalt grains in the cast alloy. Thus, significantly larger tensile stress would be required to deform the constrained cobalt filaments. In light of this, it is to be expected that the yield stress must be higher than 1000 MPa. The predicted yield strength is not precise since σ_y should increase as binder thickness decreases, whereas the values of σ_y in Table I increase with V_v at high binder contents. This is partly due to the fact that the constraining forces, as a function of binder thickness, are not precisely known.

Equation 11 indicates that the intercept is given by $G_{Ic(l)}(1 - V_v)E$. Thus, with increasing V_v , the intercept should decrease, which is contrary to observation (see Fig. 1). In the above analysis, it is assumed that $G_{Ic(l)}$ is independent of the volume fraction of cobalt. It has, however, been observed that with increasing V_v , the crack path changes from interfacial (WC/Co interface) to transgranular (WC grains). As such, $G_{Ic(l)}$ is not expected to be a constant but would increase with increasing V_v . This in part explains the increasing intercept with increasing V_v .

The important conclusion to be drawn from the present analysis is that the fundamental reason for the increase in fracture toughness of

TABLE I Estimate of σ_y of constrained binder

V_v	Slope (10^6 MPa^2)	r^2	E (GPa)	C	σ_y (MPa)
0.10	17.7	0.990	627	0.70	1270
0.16	30.2	0.993	583	0.60	1197
0.24	51.5	0.999	529	0.55	1133
0.31	102.3	0.995	490	0.45	1794
0.37	141.3	0.996	459	0.40	2023

WC-Co cermets with increasing binder thickness (at constant cobalt volume) is the increasing toughness of the binder itself due to (constrained) plane stress fracture of the binder.

2.2. Effect of microscopic residual stresses on K_{Ic}

WC-Co is fabricated by liquid-phase sintering at temperatures between 1300 and 1500°C so that the molten cobalt completely wets the tungsten carbide grains. Above the liquidus temperature, the composite is free of microscopic residual stresses. However, as the composite is cooled the cobalt binder will become essentially rigid and residual stresses will be established. Owing to the lower thermal expansion coefficient of WC as compared to cobalt, the tungsten carbide grains are put in a state of compression [23, 24] and the cobalt in tension upon cooling. These stresses are periodic in nature where the wavelength may be taken as the combined mean free path of tungsten carbide and cobalt. Although there is no specific temperature where the cobalt suddenly becomes rigid, the determination of surface stresses in the WC phase by X-ray diffraction shows the compressive stresses to range between 180 and 370 MPa when mechanical stresses are minimized [23]. Virkar and Johnson [25] showed that microscopic residual stresses can enhance the fracture toughness of ceramic-metal composites. However, the periodic nature of the residual stresses was not fully incorporated in the analysis in that internal stresses acting on only half the wavelength were considered. The effect of different elastic and thermal expansion coefficients on the stress intensity factor was also considered by Khaund *et al.* [26], but these authors did not take into account the periodic nature of residual stresses.

While the Zr-ZrO₂ composites investigated by Virkar and Johnson [25] fractured transgranularly so that the crack cut across both tension and compression regions periodically, the mode of fracture in WC-Co composites is more complex. When the mean tungsten carbide grain size (d_1) is below approximately 2 μm, the fracture occurs primarily along WC-WC interfaces [6, 27]. At large WC grain sizes (above 5 μm) the fracture is predominantly transgranular; whereas at intermediate grain sizes a mixture of intergranular and transgranular frac-

ture occurs [2, 7, 28]. At larger grain sizes the crack will have an increasing tendency to traverse transgranularly since crack deviation for intergranular fracture would be large. The following discussion of microscopic residual stresses in WC-Co also suggests that the dependence of K_{Ic} on WC grain size emerges in a natural way.

Consider a plate of unit thickness where the stress distribution can be represented by a rectangular wave. Assume that the stresses are uniform within each region. The force within a tungsten carbide grain (d_1) is exactly balanced by the force in the cobalt layer (d_2) surrounding the grain as given by a free-body diagram. Let σ_1 be the compressive stress in the WC grains and σ_2 be the tensile stress in the cobalt layer. In order to balance forces, $|\sigma_1 d_1|$ must equal $|\sigma_2 d_2|$. Although the simplest possible representation is chosen for the ease of calculations, it should be emphasized that the methodology is general and any complex residual stress distributions can be easily taken into account. The plate contains a sharp crack of length $2a$. In the absence of externally applied loads, the crack surface must be traction free. Thus, using the principle of superposition, the present problem can be expressed as a sum of two problems, one without the crack and the other (complementary) containing a crack with opposite surface tractions as shown in Fig. 2. The problem reduces to the determination of K_I for a crack loaded by periodic stresses of amplitude σ_1 and σ_2 . Half the crack length can be represented in terms of the wavelength by

$$a = d_1/2 + (m + f)\lambda \quad (12)$$

where m is an integer which represents the number of cycles, as shown in Fig. 3, f represents a fraction of a wavelength and varies between 0 and 1, and $\lambda = d_1 + d_2$. The loading of the complementary problem is shown in Fig. 3. The stress intensity factor [29] due to the residual stresses (K_I^R) is given by

$$K_I^R = \frac{1}{(\pi a)^{1/2}} \int_{-a}^{+a} \sigma(x) \left(\frac{a+x}{a-x} \right)^{1/2} dx \quad (13)$$

where $\sigma(x)$ is the stress. It can be shown that K_I^R oscillates between two extremum values depending upon the position of the crack tip. Also, for $a \gg \lambda$, K_I^R is independent of the actual

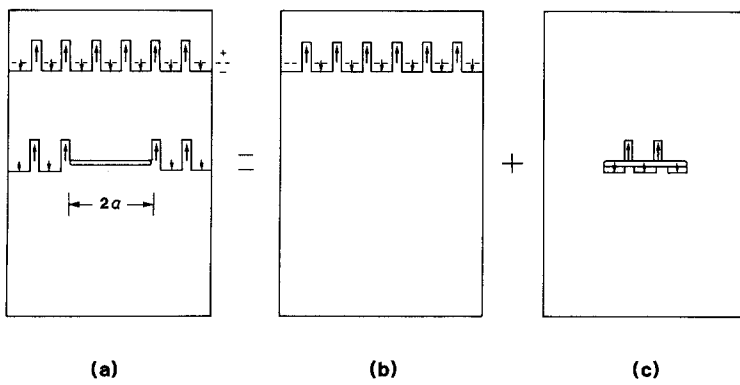


Figure 2 (a) A plate of unit thickness containing a sharp crack of length $2a$. The plate has an internal periodic stress distribution and the crack surfaces are free of tractions. (b) A crack-free plate of unit thickness with periodic internal stress distribution. (c) The complementary problem; the crack surfaces are under tractions of opposite sign. The plate contains no internal stress distribution.

magnitude of a ; it only depends upon crack tip location. That is $K_I^R \neq F(m)$ for large m , but $K_I^R = F(f)$. As shown in the Appendix, it is possible to obtain the extremum values of K_I^R . Table II gives the extremum values of K_I^R in terms of λ , d_1 or d_2 . Fig. 4 shows that the periodic stresses cause K_I^R to vary between a minimum value when the crack is about to leave the transgranularly cleaved WC particles (at the WC-Co interface) to a maximum value when it leaves the cobalt ligaments at the Co-WC interface).

If an external stress, σ_a , is applied the stress intensity factor is given by

$$K_I^a = \sigma_a(\pi a)^{1/2} \quad (14)$$

The crack will become catastrophic when the net $K_I \geq K_{Ic}^o$ or when

$$K_I^a + K_I^R \geq K_{Ic}^o \quad (15)$$

Since a tensile load is applied in mode I opening, the crack will have to overcome the compressive stresses in the WC grains before fracturing and therefore, for failure to occur, K_I^a must satisfy

$$K_I^a \geq K_{Ic}^o + A_1 \sigma_1 d_1^{1/2} \quad (16)$$

where A_1 is a constant which is dependent on the ratio d_1/d_2 (see Table II and Fig. 4) and is independent of crack length. The apparent

toughness of the composite is then given as

$$K_{Ic}^a = K_{Ic}^o + A_1 \sigma_1 (d_1)^{1/2} \quad (17)$$

The extremum values at f equal to 0 or 1 (see Table II) cause the apparent toughness to increase and are therefore the values of interest. A typical WC-Co composition used in mining applications would have a mean WC grain size near $5 \mu\text{m}$. Using Table II as a guide and assuming the compressive stresses to be 300 MPa [23] one calculates that the contribution made by the periodic stresses is nearly $1 \text{ MPa m}^{1/2}$. While the measured fracture toughness (K_I^a) reported in the literature for this material would be about $15 \text{ MPa m}^{1/2}$ [7], it is still significant that the theoretical calculations give values for K_I^R which are within an order of magnitude of K_I^a . The fact that contiguous WC grains may make d_1 larger than assumed and the crack may preferentially fracture along WC-Co interfaces and through WC grains to minimize fracture through cobalt suggests that the contribution of the microscopic residual stresses may be greater than predicted.

Since V_v can be expressed as a function of d_1 and d_2 as shown in Equation 3, at constant volume fraction of the cobalt phase, A , which is a function of d_2/d_1 , would be a constant. Thus, a plot of K_{Ic}^a against $d_1^{1/2}$ or $d_2^{1/2}$ should yield a straight line. In Fig. 5, the data of Chermant and

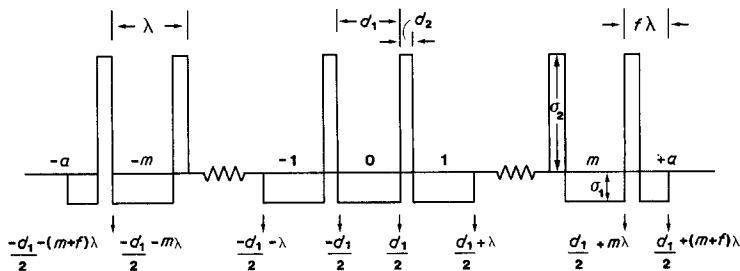


Figure 3 Surface tractions on the crack faces of length $2a = d_1 + 2(m + f)\lambda$.

TABLE II Extremum values of K_I^R

d_1/d_2	$K_I^R/\sigma_1\lambda^{1/2} = -A$		$K_I^R = -A_1\sigma_1d_1^{1/2}$ at $f = 0 = 1$	$K_I^R = A_2\sigma_2d_2^{1/2}$ at $f = d_2/\lambda$
	$f = 0 = 1$	$f = d_2/\lambda$		
1.0	-0.859	0.859	$-1.215\sigma_1d_1^{1/2}$	$1.215\sigma_2d_2^{1/2}$
2.5	-1.005	1.682	$-1.189\sigma_1d_1^{1/2}$	$1.259\sigma_2d_2^{1/2}$
5.0	-1.077	2.644	$-1.180\sigma_1d_1^{1/2}$	$1.295\sigma_2d_2^{1/2}$
10.0	-1.120	4.080	$-1.175\sigma_1d_1^{1/2}$	$1.353\sigma_2d_2^{1/2}$
15.0	-1.136	5.185	$-1.173\sigma_1d_1^{1/2}$	$1.384\sigma_2d_2^{1/2}$

Osterstock [6, 7] are plotted against $d_1^{1/2}$. The linear relationship of the experimental data at constant volume fraction of cobalt indicates that microscopic residual stresses make a more significant contribution than the theoretical predictions suggest.

It should be emphasized that, in the strictest sense, dependence of K_{Ic} cannot be expressed in terms of the mean free path in cobalt since the crack would like to traverse the minimum possible distance in cobalt due to the high toughness of the cobalt phase. In the above calculations, it was decided to refer to d_2 as the mean free path since actual distance traversed by a crack in the cobalt layer will be proportional to the mean free path, d_2 .

There are at least two factors that contribute to the increasing fracture toughness of the composite material as the WC grain size becomes larger. First, the mean free path of cobalt increases and this increases the toughness, as was discussed earlier; secondly, the increasingly transangular nature of the fracture causes the fracture toughness to increase as the volume per

cent cobalt increases or as the grain size increases due to the microscopic residual stresses. The slope of the 37% cobalt is larger than the slope of the 10% cobalt compositions in Fig. 5. This is to be expected since the magnitude of σ_1 should increase with increasing V_v .

When the WC grain size is small ($< 2 \mu\text{m}$) and the cobalt levels are low (i.e. 10 vol %) fracture occurs primarily along apparently contiguous WC-WC grains. The contribution of microscopic residual stresses is therefore small. As the binder film thickness increases, due to increasing WC grain size, fracture of the WC grains becomes easier than crack deviation which would allow interfacial fracture. The effect of periodic residual stresses is therefore most predominant at large WC grain sizes.

As additional proof that microscopic residual stresses in commercial grades of WC-Co contribute to the measured fracture toughness, two compositions were annealed in vacuum at 600°C for 1 h. The magnetic saturation of the samples was measured before and after annealing, which revealed that the binder chemistry

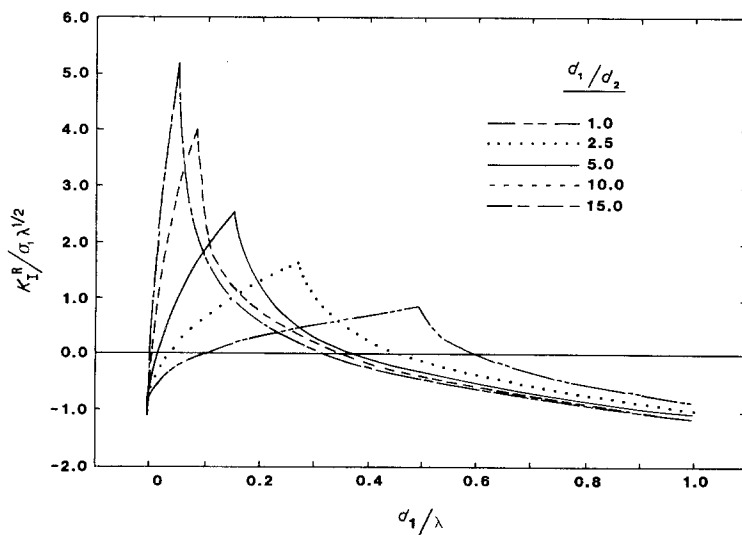


Figure 4 Variation in stress intensity factor (K_I^R) due to periodic internal stresses for various ratios of carbide grain size (d_1) to binder film thickness (d_2).

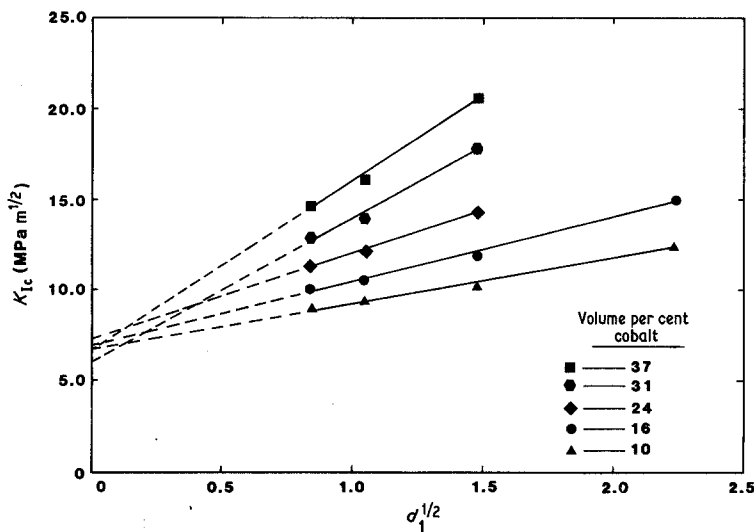


Figure 5 Data of Chermant and Osterstock [6, 7] are plotted to show the linear relationship which results when K_{Ic} is plotted against $d_1^{1/2}$. Note the increasing slope with cobalt volume fraction.

was unchanged and did not affect the fracture toughness measurements [30]. Table III shows that in both cases the fracture toughness decreases upon annealing a portion of the internal residual stresses. The contribution of the residual stresses to the fracture toughness is larger than the data in Table III suggest since stresses were introduced by cooling from 600°C.

In Equation 17, K_{Ic}° is the fracture toughness of the cermet in the absence of internal periodic stresses. K_{Ic}° , however, is not a constant but is given by:

$$K_{Ic}^{\circ} \approx (2G_{Ic(1)}E)^{1/2} \left(1 + \frac{\sigma_y d_2^2}{3G_{Ic(1)}d_1} \right)^{1/2} \quad (18)$$

For $V_v \ll 1$ and $\sigma_y d_2^2 / (3G_{Ic(1)}d_1) \ll 1$ then

$$K_{Ic}^{\circ} \approx (2G_{Ic(1)}E)^{1/2} \left(1 + \frac{\sigma_y d_2^2}{6G_{Ic(1)}d_1} \right) \quad (19)$$

Therefore, K_{Ic}° is not a constant but varies with

d_1 . Since $d_2/d_1 = \text{constant}$ for a given volume fraction,

$$K_{Ic}^{\circ} \approx (2G_{Ic(1)}E)^{1/2} \left(1 + \frac{\alpha \sigma_y d_2}{6G_{Ic(1)}} \right) \quad (20)$$

where $\alpha = (d_2/d_1) = \text{constant}$. For very small V_v , however, K_{Ic}° is nearly a constant since $[\sigma_y d_2^2 / 6G_{Ic(1)}d_1] \ll 1$.

K_{Ic}° against $d_1^{1/2}$ plots in Fig. 5 indicate that the intercept indeed is nearly the same for all volume fractions. For volume fractions greater than 0.1, however, the assumption of $V_v \ll 1.0$ is not very accurate. Despite this, it is interesting to see that the intercept indeed is nearly constant.

2.3. Effect of macroscopic residual stresses on K_{Ic}

2.3.1. Experimental results

Prior work [31] has shown that residual stresses on a macroscopic scale can be introduced in

TABLE III Partial relief of internal residual stresses by annealing

Composition ^a	Time annealed at 600°C (h)	Magnetic saturation ^b (emu/g)	K_{Ic}° (MPa m ^{1/2})	
			\bar{x}^d	s^e
WC-9Co ^f	0	12.39	12.79	0.08
	1	12.47	12.13	0.15
WC-9Co ^g	0	12.49	14.07	0.12
	1	12.36	13.44	0.14

^aSupplied by Multi-Metals Division, Vermont American Corporation, Louisville, KY, USA.

^bDetermined using Model SM 8100 (LDJ Electronics, Troy, MI, USA) saturation induction measuring system.

^cDetermined using short-rod technique [18].

^dMean value of 3-5 measurements.

^eStandard deviation.

^fGrade 0M1 (mean WC grain size of 2-3.5 μm), Rockwell A hardness of 90.0 ± 0.5.

^gGrade 25M1 (mean WC grain size of 6-8 μm), Rockwell A hardness of 88.0 ± 0.5.

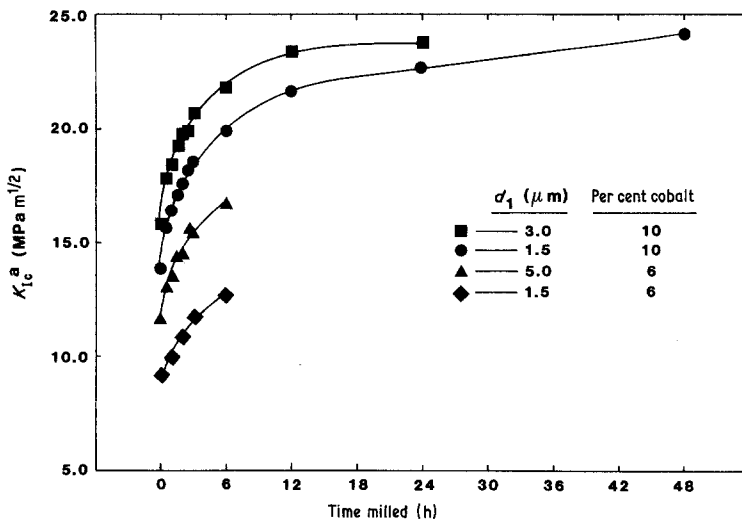


Figure 6 Variation in apparent toughness with milling time for WC-6Co and WC-10Co grades with mean WC grain sizes of 1.5, 3.0 and 5.0 μm . Note that surface compressive stresses increase with milling time.

WC-Co cermets by impacting sintered specimens against one another in an attritor or a ball mill. In order to explore the effect of such macroscopic stresses, commercially prepared WC-6Co (6 wt % Co) and WC-10Co[§] short-rod specimens (12.7 mm diameter by 19.1 mm long) were tumbled in a 15.2 cm diameter stainless-steel ball mill. The mill, which operated at 75 r.p.m. was charged with 14.5 kg WC-Co drilling inserts (15.9 mm diameter by approximately 20.3 mm long) and 1500 ml acetone. Chevron-notched slots were cut with a diamond saw and testing was performed as described previously [18, 30]. Selected samples were strain-gauged[¶] before breaking. Fractured samples were ground and polished to a 1 μm finish and were indented using a Vicker's diamond pyramid indenter on a universal testing machine.*

The fracture toughness of 6 and 10% cobalt composites, as a function of milling time, for different WC grain sizes are shown in Fig. 6. All four grades required higher loads to fracture after the tumbling process which deformed the cobalt near the surface of the specimens, thereby establishing a surface compressive stress. The per cent increase in fracture toughness is nearly the same regardless of the cobalt content or WC grain size. Barker [18], while explaining that K_{Ic} is a material parameter that is independent of macroscopic residual stresses, showed that small macroscopic stresses could be corrected for by unloading during the test and determining

graphically a residual stress factor, r , as shown in Fig. 7. Barker found the apparent toughness (K_{Ic}^a) to be given by

$$K_{Ic}^a = \beta P_m / b^{3/2} \quad (21)$$

where β is a constant determined by the geometry of the specimen, P_m is the load on the specimen at the critical location (location where the maximum load occurs) and b is the specimen diameter. The residual stress factor, r , has been derived analytically and shown experimentally to correct for small residual stresses in the relation [18]

$$K_{Ic} = \frac{\beta P_m}{b^{3/2}} \left(\frac{1+r}{1-r} \right)^{1/2} \quad (22)$$

The fact that the residual stress factor, r , correlates with the increasing compressive stresses is clearly shown in Fig. 8. The presence of compressive stresses on the outer surface was also confirmed by the fact that indentation cracks (which were mainly Palmqvist cracks) were shorter on the outer surface compared to that on the inner surface which had a balancing tensile stress (see Fig. 9). Strain gauges further confirmed the existence of compressive stresses on the outer surface and tensile stresses on the inner surface. Substantial residual stresses were observed at depths up to 100 μm . Compressive stresses near the surface of specimens are advantageous in rock drilling applications where inserts are loaded in compression but fail due to contact tensile stresses.

[§]Supplied by Hughes MPD, Houston, TX, USA.

[¶]PA-06-062AG-350, Magnaflex Products, Chicago, IL, USA.

*Model 1125, Instron Corp, Canton, MA, USA.

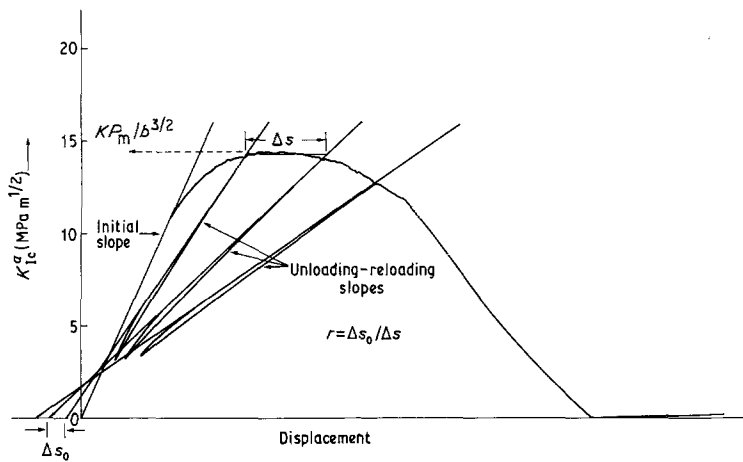


Figure 7 Determination of residual stress factor r from test record. WC-6Co specimen was milled for 1.5 h. $K_I^a = 14.3 \text{ MPa m}^{1/2}$ and $r = -0.22$.

2.3.2. Modelling of residual stresses

Fig. 10 shows that the true K_{Ic} can be obtained by correcting for the residual stresses for values of $r \leq |0.15|$ as previously determined by Barker [18]. Although for a complex specimen geometry of the short-rod specimen, a phenomenological approach for incorporating the macroscopic residual stresses is necessary, it is possible to incorporate the effect of residual stresses analytically for simpler sample geometries. In the following, an analysis of residual stresses is presented for a double cantilever beam (DCB) specimen wherein it is assumed that the length of the crack is much greater than the thickness of the sample. The residual stress distribution for the tumbled specimens can be modelled as shown in Fig. 11 in which a DCB sample with compressive stress of magnitude σ_c exists[†] in the outer region to a depth of λ . The

residual stresses must be exactly balanced and can be given as

$$\sigma_c \lambda = \sigma_t (d - \lambda) \quad (23)$$

where σ_t is the tensile stress, d is one-half the specimen thickness and b is the width. The bending moment due to the residual stresses, M_R , is calculated as:

$$M_R = b \int_{d-\lambda}^d \sigma_c y \, dy - b \int_0^{d-\lambda} \sigma_t y \, dy \quad (24)$$

which upon integration gives

$$M_R = \sigma_c \lambda b d / 2 \quad (25)$$

Analysis of bending of the lower beam in Fig. 11 consists of adding the moment due to residual stresses to the moment resulting from the applied load, M_A , to give the bending moment, M , as

$$M = M_A + M_R = Px - \sigma_c \lambda b d / 2 \quad (26)$$

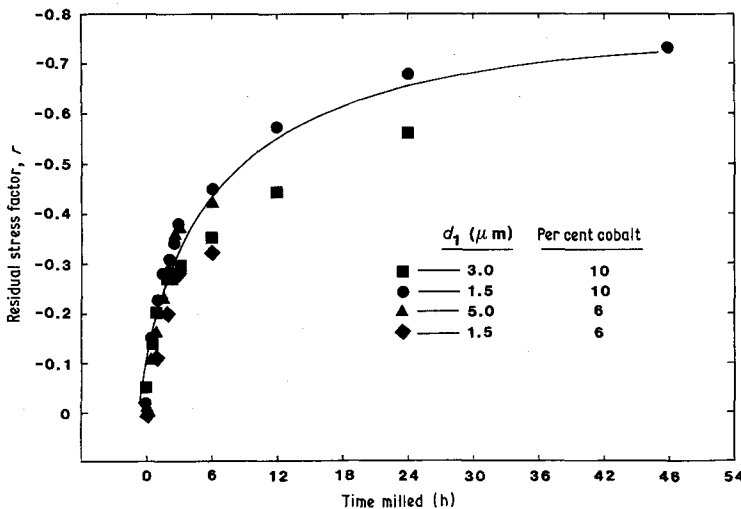


Figure 8 Residual stress factor r as a function of milling time. Note that r becomes more negative with increasing milling time (i.e. with increasing compressive stresses).

[†]Here, σ_c is the positive value of the compressive stress.

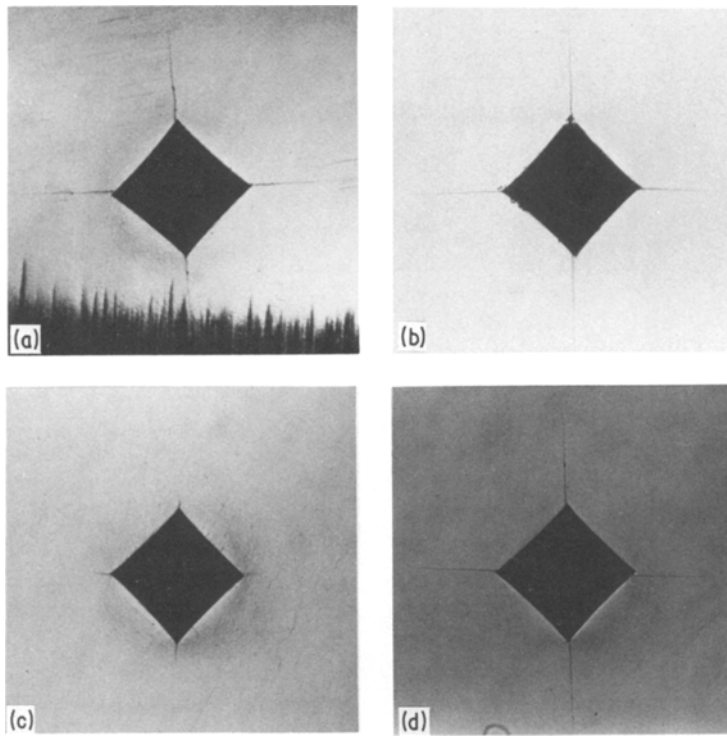


Figure 9 Vicker's indentations made at 890 N on fractured WC-6Co short-rod specimens. Specimens (a) and (b) were as-received and specimens (c) and (d) were identical except that they were milled for 24 h in order to introduce large surface stresses. (a) Indent on the surface of as-received specimen. (b) Indent on the central part of as-received specimen. (c) Indent on the surface of milled specimen. (d) Indent on the central part of milled specimen. Note that Palmqvist cracks in both (a) and (b) are approximately of the same length, indicating minimal residual stresses in these specimens; while crack lengths in (c) are much shorter than in (d), showing that large compressive surface stresses exist in these specimens.

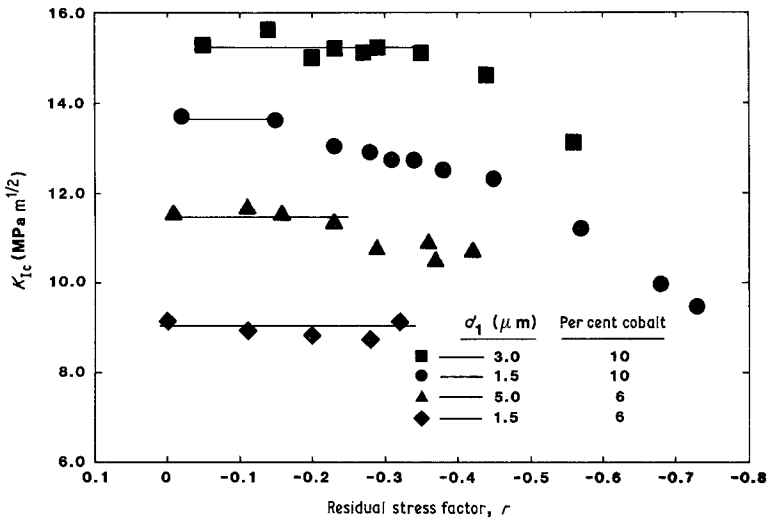


Figure 10 K_{Ic} calculated using Equation 22 as a function of r . Data show that it is only possible to correct for the residual stresses using Equation 22 for $r \leq |0.15|$.

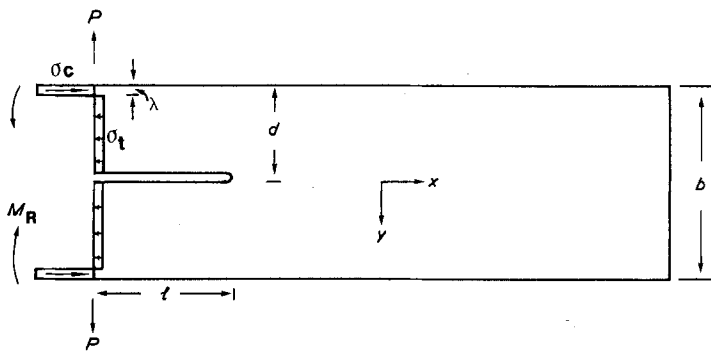


Figure 11 DCB-type specimen showing assumed residual stress distribution and applied load. Large compressive stresses exist at the surface and are balanced by smaller tensile stresses in the centre.

Here M_R is given by $-\sigma_c \lambda b d / 2$ since its sense is opposite to M_A . The strain energy, U , is given as

$$U = \int_0^l \frac{M^2}{2EI} dx \quad (27)$$

where E is Young's modulus and I is the moment of inertia of the cross-section. Integrating Equation 27 gives

$$U = \frac{1}{2EI} \left(\frac{P^2 l^3}{3} + \frac{\sigma_c^2 \lambda^2 b^2 d^2 l}{4} - \frac{P \sigma_c \lambda b d l^2}{2} \right) \quad (28)$$

For crack extension to occur

$$\frac{\partial U}{\partial l} \geq \frac{\partial S}{\partial l} \quad (29)$$

where S is the surface energy which is equal to $\gamma b l$, γ being the fracture energy. Substituting Equation 28 into Equation 29 results in

$$\frac{P^2 l^2}{Ib} - \frac{P \sigma_c \lambda b d l}{Ib} + \frac{\sigma_c^2 \lambda^2 b^2 d^2}{4Ib} \geq 2\gamma E \quad (30)$$

which can be written as

$$(K_I^a)^2 - K_I^a \sigma_c \lambda d \left(\frac{b}{I} \right)^{1/2} + \frac{\sigma_c^2 \lambda^2 b d^2}{4I} - \left(K_{Ic}^o \right)^2 \geq 0 \quad (31)$$

where K_{Ic}^o is equal to $(2\gamma E)^{1/2}$ which is the fracture toughness in the absence of macroscopic residual stresses. (Here, K_{Ic}^o represents K_{Ic}^a in the absence of macroscopic residual stresses. Microstructural effects such as the binder thickness effects and internal periodic stress effects are included in K_{Ic}^o .) Solving for the critical value of the apparent toughness in Equation 30 gives

$$K_{Ic}^a = K_{Ic}^o + \frac{\sigma_c \lambda d}{2} \left(\frac{b}{I} \right)^{1/2} \quad (32)$$

When surface compressive stresses are present, the apparent toughness is always higher than the material property K_{Ic}^o , which is in accordance with the present results. (If the surface layer were to consist of a tensile stress, K_{Ic}^a would be lower than K_{Ic}^o .)

Furthermore, Equation 32 agrees with the K_I approach used in the previous section. The stress intensity factor due to macroscopic compressive stress is given as

$$K_I^R = \frac{M_R}{(bI)^{1/2}} = -\frac{\sigma_c \lambda b d}{2(bI)^{1/2}} \quad (33)$$

Since for crack extension to occur, $K_I^a + K_I^R \geq K_{Ic}^o$, the apparent toughness is given as

$$K_{Ic}^a \geq K_{Ic}^o + \frac{\sigma_c \lambda d}{2} \left(\frac{b}{I} \right)^{1/2} \quad (34)$$

which is identical to Equation 32.

In order to examine the deflection δ_R of the beam due to the residual stresses, the bending of the lower beam in Fig. 11 can be found by solving

$$\frac{d^2 y}{dx^2} = \frac{M}{EI} = \frac{Px}{EI} - \frac{\sigma_c \lambda b d}{2EI} \quad (35)$$

Integrating the right-hand side of Equation 35 twice and determining the constants of integration knowing that $y = 0$ at $x = l$ gives

$$y = \frac{Px^3}{6EI} - \frac{Pl^2 x}{2EI} + \frac{\sigma_c \lambda b d l x}{2EI} - \frac{\sigma_c \lambda b d x^2}{4EI} + \frac{Pl^3}{3EI} - \frac{\sigma_c \lambda b d l^2}{4EI} \quad (36)$$

The deflection, δ , as measured at $x = 0$ (see Fig. 11) is given as

$$\delta = \frac{Pl^3}{3EI} - \frac{\sigma_c \lambda b d l^2}{4EI} \quad (37)$$

The above analysis suggests that upon unloading after some crack extension, the extrapolation of the load–deflection curve to zero load will yield a negative intercept. Consider a sample with an initial crack length of l_0 . If the crack extends to length l , then upon unloading, the intercept will be negative and given by

$$\delta_R - \delta_{R(0)} = -\frac{\sigma_c \lambda b d}{4EI} (l^2 - l_0^2) \quad (38)$$

The negative sign indicates that with reference to the origin the extrapolated deflection is actually opposite to that created by the applied load.

2.3.3. Chevron-notched DCB specimen: analysis of residual stresses

Incorporation of macroscopic residual stresses in the analysis of the short-rod specimen is a complex problem. A detailed numerical analysis would be required. However, several salient features of these effects in a short-rod (or bar) type of specimen may be easily elucidated by analysing a DCB sample with chevron notch as shown in Fig. 12. The residual stress distribution in Fig. 12 is as shown in Fig. 11. In the following analysis, we will assume that $l \gg d$ so that bending energy of the beam is much greater than shear energy as well as energy stored in regions past the crack tip.

Let us first examine the specimen characteristics in the absence of residual stresses. The surface energy when crack extension occurs is given by:

$$S = \gamma \tan \alpha (l - l_0)^2 \quad (39)$$

The condition for crack extension is given by

$$\frac{dU}{dl} \geq \frac{dS}{dl} \quad (40)$$

which results in

$$\frac{P^2 l^2}{2EI} \geq 2\gamma \tan \alpha (l - l_0) \quad (41)$$

The maximum load, $P_{m(0)}$, is given by $dP/dl = 0$, which results in the following relationships for maximum load and $l_{m(0)}$, the crack length at the maximum load:

$$P_{m(0)} = \left(\frac{\gamma EI \tan \alpha}{l_0} \right)^{1/2} \quad (42)$$

and

$$l_{m(0)} = 2l_0 \quad (43)$$

With the residual stress distribution shown in Fig. 11 the condition for crack extension is now given by

$$\frac{1}{2EI} \left(p^2 l^2 + \frac{\sigma_c^2 \lambda^2 b^2 d^2}{4} - P \sigma_c \lambda b d l \right) \leq 2\gamma \tan \alpha (l - l_0) \quad (44)$$

or

$$P^2 - \frac{P \sigma_c \lambda b d}{l} + \frac{\sigma_c^2 \lambda^2 b^2 d^2}{4l^2} - \frac{4\gamma EI \tan \alpha (l - l_0)}{P} \geq 0 \quad (45)$$

and

$$P = \frac{\sigma_c \lambda b d}{2l} + 2(\gamma EI \tan \alpha)^{1/2} \frac{(l - l_0)^{1/2}}{l} \quad (46)$$

The maximum value of P is again determined by setting $dP/dl = 0$ which results in the following relationship for the crack length at the maximum load:

$$(l_m - l_0)^{1/2} = \frac{1}{2} \left[\left(4l_0 + \frac{\sigma_c^2 \lambda^2 b^2 d^2}{4\gamma EI \tan \alpha} \right)^{1/2} - \frac{\sigma_c \lambda b d}{(4\gamma EI \tan \alpha)^{1/2}} \right] \quad (47)$$

i.e. maximum in load occurs at a shorter crack length. Note that if $\sigma_c = 0$, $l_m = 2l_0$ as given in Equation 43. Confirmation of the shift in crack position at maximum load with increasing residual compressive stresses was made on short-rod WC–Co specimens by loading to the critical location, marking the crack location with a dye and then fracturing through the specimen. A shorter value of l_m for specimens milled 24 h as compared to unmilled control specimens agrees with the general trend suggested by Equation 47 as compared to Equation 43. This observation suggests that compliance calibrations used in determining crack length for

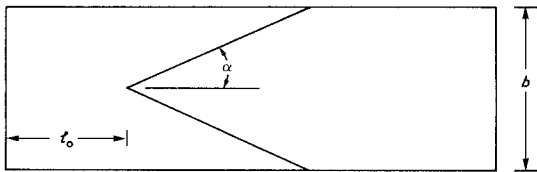


Figure 12 Chevron-notched DCB-type specimen showing chevron-shaped crack front of angle 2α .

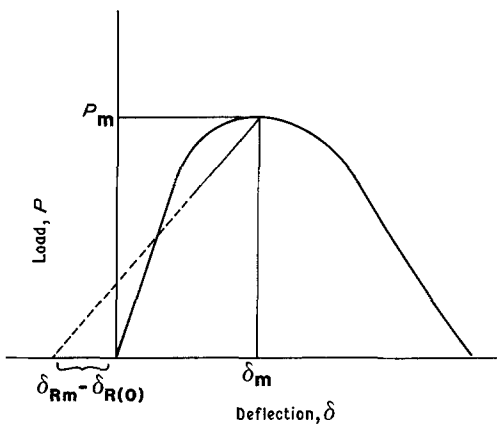


Figure 13 Predicted load-deflection trace for chevron-notched DCB-type specimen with surface compressive stresses. The figure also shows negative intercept that results upon unloading subsequent to some crack extension.

relationship:

$$K_{Ic}^{\circ} = \frac{\sigma_c \lambda b d [(3\delta_m EI/P_m)^{1/3} - l_0]^{1/2}}{2[2l_0 - (3\delta_m EI/P_m)^{1/3}] (2I \tan \alpha)^{1/2}} \quad (50)$$

The only unknown quantity is the product $\sigma_c \lambda$. If we assume that we can unload as soon as the load has reached its maximum value (see Fig. 13), we obtain the deflection δ_{Rm} at the maximum load as

$$\delta_{Rm} - \delta_{R(0)} = \frac{\sigma_c \lambda b d}{4EI} (l_m^2 - l_0^2) \quad (51)$$

Therefore

$$\sigma_c \lambda = \frac{4EI}{bd} \frac{|\delta_{Rm} - \delta_{R(0)}|}{(3EI\delta_m/P_m)^{2/3} - l_0^2} \quad (52)$$

Substituting Equation 52 in Equation 50 gives

$$K_{Ic}^{\circ} = \frac{2EI|\delta_{Rm} - \delta_{R(0)}| [(3EI\delta_m/P_m)^{1/3} - l_0]^{1/2}}{[(3EI\delta_m/P_m)^{2/3} - l_0^2] (2I \tan \alpha)^{1/2} [2l_0 - (3\delta_m EI/P_m)^{1/3}]} \quad (53)$$

samples with minimal macroscopic residual stresses ($r \leq |0.15|$) cannot be used when substantial stresses are present.

The magnitude of the maximum load can be shown to be given by

$$P_m = \frac{1}{l_m} \left\{ \frac{\sigma_c \lambda b d}{2} + (\gamma EI \tan \alpha)^{1/2} \times \left[\left(4l_0 + \frac{\sigma_c^2 \lambda^2 b^2 d^2}{4\gamma EI \tan \alpha} \right)^{1/2} - \frac{\sigma_c \lambda b d}{(4\gamma EI \tan \alpha)^{1/2}} \right] \right\} \quad (48)$$

The load therefore increases with increasing surface compressive stresses. Since K_{Ic}^a is determined from the maximum in load in the chevron-notch type of specimens, the K_{Ic}^a so determined will be greater than the true K_{Ic}° . The objective clearly will be to determine K_{Ic}° from the measured K_{Ic}^a . A graphical method, however, can be used to evaluate K_{Ic}° from the load-deflection chart. Fig. 13 shows a schematic of the load-deflection plot. The deflection δ_m at the maximum load is:

$$\delta_m = \frac{P_m l_m^3}{3EI} \quad (49)$$

Thus solving for l_m and setting it equal to l_m in Equation 47 results in the following

All of the quantities in the above equation are known. Thus, in principle the material property, K_{Ic}° , can be evaluated from the data obtained during a test (see Fig. 13). If $\sigma_c \lambda$ equals zero then Equation 53 is indeterminate and l'Hospital's rule must be employed.

The analysis presented above, however, is not quantitatively applicable to the short-rod specimen since the crack length is comparable to the diameter, and not much greater as assumed in the analysis. Furthermore, in the analysis the cross-sectional area of the sample was assumed to be rectangular. A cylindrical geometry creates a somewhat more complicated stress distribution than assumed in the analysis. Even so, trends predicted by the analysis, namely (i) increase in P_m with increasing surface compressive stresses with corresponding decrease of l_m and (ii) negative extrapolated intercept on the deflection axis, are confirmed experimentally on the short-rod specimen. Fig. 7 shows an actual trace of a short-rod specimen which had been milled for 1.5 h. If the residual stresses are low ($r \leq |0.15|$) then Equation 22 may be used as an approximation. Equation 53 is useful when substantial macroscopic residual stresses are present for chevron-notched DCB specimens. Experimentally, there may be some difficulty unloading

precisely at P_m . This difficulty can be circumvented by unloading several times and plotting P vs $(\delta_R - \delta_{R(0)})$ and graphically determining $(\delta_{Rm} - \delta_{R(0)})$.

3. Discussion and conclusions

The present work has shown that the increase in K_{Ic} with increasing WC grain size at fixed volume fraction of the cobalt phase can be explained on the basis of two independent factors. First, the increase in WC grain size correspondingly increases the thickness of the cobalt layer. Failure of constrained cobalt occurs by a plane stress mechanism wherein the toughness of cobalt itself increases with increasing thickness. Secondly, the internal periodic residual stresses arising out of thermal mismatch between WC and cobalt contribute to the toughness. This contribution also increases with increasing WC grain size at fixed volume fraction of the cobalt phase. It is difficult at present to separate the two contributions fully based on the available data. However, with increasing WC grain size, even if average thickness of cobalt layer increases, the crack will invariably take the path of least resistance. Thus, the crack will tend to avoid regions locally rich in cobalt and the actual thickness effect would be less than predicted by the present analysis. By contrast, the contribution of the internal periodic residual stresses would increase with increasing WC grain size despite inhomogeneous distribution of cobalt since it is WC which is under compression. Thus, if the crack avoids cobalt rich regions, the transgranular fracture of WC would correspondingly increase. For the internal periodic stress effects to be dominant, however, it is essential that the failure be predominantly transgranular. Since the failure becomes increasingly transgranular with increasing WC grain size, it is expected that the effect of internal stresses would increase with increasing WC grain size.

It has been shown that macroscopic compressive residual stresses near the surface of the WC-Co composite can increase the apparent fracture toughness. A simple model describing the residual stress distribution quantitatively shows that the maximum load in the short-rod or chevron DCB test increases, while the crack location at the peak load decreases with increasing compressive stresses near the surface of the

composite. A graphical technique can be used to determine the true fracture toughness of the composite (free of residual stress effects). While it must be realized that binder thickness and residual stresses are not the only factors affecting the fracture toughness of WC-Co composites, it has been shown that the contribution of these factors to fracture toughness can be significant in explaining microstructure-toughness relationships.

Appendix

Calculation of extremum values of K_I^R

Referring to Fig. 3 it is seen that $\sigma(x) = -\sigma_1$ when

$$[d_1/2 + id_2 + (i-1)d_1] < x < (d_1/2 + id_2 + id_1)$$

where i is an integer such that $-m \leq i \leq m$ and $\sigma_1 > 0$. Similarly $\sigma(x) = \sigma_2$ when

$$(d_1/2 + id_1 + id_2) < x < [d_1/2 + id_1 + (i+1)d_2]$$

where $-m \leq i \leq (m-1)$ and $\sigma_2 > 0$. Equation 13 therefore becomes

$$K_I^R = \frac{1}{(\pi a)^{1/2}} \left[-\sigma_1 \sum_{j=0}^{j=2m} \int_{-d_1/2-(m-j)(d_1+d_2)}^{-d_1/2-(m-j)d_2-[m-(j+1)]d_1} \left(\frac{a+x}{a-x} \right)^{1/2} dx + \sigma_2 \sum_{k=0}^{k=(2m-1)} \int_{-d_1/2-(m-k)d_2-[m-(k+1)]d_1}^{-d_1/2-[m-(k+1)](d_1+d_2)} \left(\frac{a+x}{a-x} \right)^{1/2} dx \right] \quad (A1)$$

when f is equal to zero or one. The integral can easily be evaluated since

$$\int \left(\frac{a+x}{a-x} \right)^{1/2} dx = a \left\{ \sin^{-1} \left(\frac{x}{a} \right) - \left[1 - \left(\frac{x}{a} \right)^2 \right]^{1/2} \right\} \quad (A2)$$

When $f < d_2/(d_1 + d_2)$ then the following must be added to Equation A1 in order to obtain K_I^R .

$$K_I = \frac{\sigma_2}{(\pi a)^{1/2}} \left[\int_{-a}^{-d_1/2-m(d_1+d_2)} \left(\frac{a+x}{a-x} \right)^{1/2} dx + \int_{d_1/2+m(d_1+d_2)}^a \left(\frac{a+x}{a-x} \right)^{1/2} dx \right] \quad (A3)$$

When $f > d_2/(d_1 + d_2)$ then K_I^R is obtained by

adding Equation A1 and the following:

$$K_I = \frac{1}{(\pi a)^{1/2}} \left\{ \sigma_2 \left[\int_{-d_1/2 - m(d_1 + d_2) - d_2}^{-d_1/2 - m(d_1 + d_2)} \left(\frac{a+x}{a-x} \right)^{1/2} dx + \int_{d_1/2 + m(d_1 + d_2)}^{d_1/2 + m(d_1 + d_2) + d_2} \left(\frac{a+x}{a-x} \right)^{1/2} dx \right] - \sigma_1 \left[\int_{-a}^{-d_1/2 - m(d_1 + d_2) - d_2} \left(\frac{a+x}{a-x} \right)^{1/2} dx - \int_{d_1/2 + m(d_1 + d_2) + d_2}^a \left(\frac{a+x}{a-x} \right)^{1/2} dx \right] \right\} \quad (A4)$$

The extremum values of K_I^R in principle can be obtained by setting

$$\frac{dK_I^R}{df} = 0 \quad (A5)$$

This procedure is analytically too complex. However, numerically it can easily be shown that the extremum values occur at $f = 0 = 1$ and $f = d_2/\lambda$. Let $Z(x) = \sin^{-1}(x/a) - [1 - (x/a)^2]^{1/2}$ and $q = d_1/d_2$ so that $\sigma_2 = q\sigma_1$. The extremum value at $f = 0 = 1$ is given by:

$$K_I^R = -\sigma_1 \lambda^{1/2} \left[\left(\frac{d_1/2 + m(d_1 + d_2)}{\pi(d_1 + d_2)} \right)^{1/2} \times \left(\sum_{j=0}^{2m} \{ Z(-d_1/2 - (m-j)d_2 - [m - (j+1)]d_1) - Z[-d_1/2 - (m-j)(d_1 + d_2)] \} - q \sum_{k=0}^{2m-1} \{ Z(-d_1/2 - [m - (k+1)](d_1 + d_2)) - Z(-d_1/2 - (m-k)d_2 - [m - (k+1)]d_1) \} \right) \right] \quad (A6)$$

Intuitively it would appear that the contribution of the residual stress should be independent of crack length as long as crack length is much greater than λ . Otherwise it would imply that fracture toughness is dependent on crack length. Thus the modulus of the terms in large square brackets must converge to a constant value for large values of m . Numerical calculations show that this indeed is the case for $m \geq 5$. Values of this constant at different d_1/d_2 ratios are given in Table II.

Similarly the extremum value for $f = d_2/\lambda$ is given by

$$K_I^R = -\sigma_1 \lambda^{1/2} \times \left[\left(\frac{d_1/2 + d_2 + m(d_1 + d_2)}{\pi(d_1 + d_2)} \right)^{1/2} \times \left\{ \sum_{j=0}^{2m} \{ Z(-d_1/2 - (m-j)d_2 - [m - (j+1)]d_1) - Z(-d_1/2 - (m-j)(d_1 + d_2)) \} - q \left(\sum_{k=0}^{2m-1} \{ Z(-d_1/2 - [m - (k+1)](d_1 + d_2)) - Z(-d_1/2 - (m-k)d_2 - [m - (k+1)]d_1) \} + Z(a) - Z(b) + Z(-b) - Z(-a) \} \right) \right\} \right] \quad (A7)$$

where $b = a - d_2$. Again the term in square brackets converges with values as given in Table II. The variation of K_I^R as a function of crack location is shown in Fig. 4.

For a crack under compression with crack surfaces touching each other, the concept of a negative stress intensity factor has no meaning. However, if the crack surfaces do not touch each other at the instant the crack becomes critical under an externally applied load, the contribution of compressive stresses to the stress intensity factor is simply subtracted from the K from the applied load. In the above analysis it has been tacitly assumed that the crack surfaces do not touch each other at the condition of criticality. If the crack surfaces are indeed in contact, the analysis should include crack closure effects [32].

Acknowledgements

This work was supported in part by Sandia National Laboratories under the direction of J. Finger and the National Science Foundation under grant DMR79-12668. Discussions with Professor J. R. Rice of Harvard University and L. E. Pope and L. M. Barker of Sandia National University Laboratories are appreciated. The assistance of J. Bohman and A. MacLeod of Terra Tek, Inc, in the experimental testing and manuscript preparation, respectively, is gratefully acknowledged. The donation of commercial WC-Co materials for annealing studies by J. Tingle of Vermont American Corp (Multi-Metals Division) and for macroscopic

residual stress experiments by R. Staudenmeyer of Hughes MPD helped make these studies possible. The grinding of sintered WC-Co cylinders by J. Peters of MTC Corp is appreciated.

References

1. P. KENNY, *Powder Metall.* **14** (1971) 22.
2. S. S. YEN, MS thesis, Lehigh University, Bethlehem, PA (1971).
3. N. INGELSTROM and H. NORDBERG, *Eng. Fract. Mech.* **6** (1974) 597.
4. R. C. LUETH, PhD dissertation, Michigan State University, East Lansing, MI (1972).
5. *Idem.*, "Fracture Mechanics of Ceramics", edited by R. C. Bradt, D. P. H. HASSELMAN and F. F. Lange, Vol. 2 (Plenum Press, New York and London, 1974) p. 791.
6. J. L. CHERMANT and F. OSTERSTOCK, *J. Mater. Sci.* **11** (1976) 1939.
7. *Idem.*, Second European Colloquium on Fracture, Darmstadt, October 9–11, 1978 (Verein Deutscher, Ingenieur Zeitschriften, 1979) p. 244.
8. M. J. MURRAY, *Proc. R. Soc. A* **356** (1977) 483.
9. J. R. PICKENS and J. GURLAND, *Mater. Sci. Eng.* **33** (1978) 135.
10. J. R. RICE and M. A. JOHNSON, "Inelastic Behavior of Solids", edited by M. F. Kanninen, W. Adler, W. Rosenfield and R. Jaffe (McGraw-Hill, New York, 1974) p. 641.
11. R. K. VISWANADHAM, T. S. SUN, E. F. DRAKE and J. A. PECK, *J. Mater. Sci.* **16** (1981) 1029.
12. E. A. ALMOND, "Science of Hard Materials", edited by R. K. Viswanadham, D. J. Rowcliffe and J. Gurland (Plenum Press, New York and London, 1983) p. 517.
13. R. W. RICE, *ibid.* p. 631.
14. S. B. LUYCKX, *ibid.* p. 583.
15. B. ROEBUCK, *J. Mater. Sci.* **14** (1979) 2837.
16. S. OHMAN, E. PARNAMA and S. PALMQUIST, *Jernkont. Ann.* **151** (1967) 126.
17. J. E. FARB, MS thesis, University of Utah, Salt Lake City, UT (1978).
18. L. M. BARKER, "Advances in Fracture Research", edited by D. Francois, Vol. 5 (1981) p. 2563.
19. G. R. IRWIN, J. A. KIES and H. L. SMITH, *Proc. Amer. Soc. Test. Mater.* **58** (1958) 640.
20. J. F. KNOTT, "Fundamentals of Fracture Mechanics" (Wiley, New York and Toronto, 1973) p. 114.
21. I. JOHANSSON and L. E. GUSTAVSSON, Sandvik Coromant Laboratory Report No. 2246.
22. W. DAWIHL and B. FRISCH, *Cobalt* **22** (1964) 22.
23. D. N. FRENCH, *J. Amer. Ceram. Soc.* **52** (1969) 267.
24. B. O. JAENSSON, *Mater. Sci. Eng.* **8** (1971) 41.
25. A. V. VIRKAR and D. L. JOHNSON, *J. Amer. Ceram. Soc.* **60** (1977) 514.
26. A. K. KHAUND, V. D. KRSTIC and P. S. NICHOLSON, *J. Mater. Sci.* **12** (1977) 2269.
27. C. LEA and B. ROEBUCK, *Met. Sec.* **6** (1981) 262.
28. S. B. LUYCKX, *Acta Metall.* **16** (1968) 535.
29. G. C. SIH, "Handbook of Stress Intensity Factors", (Institute of Fracture and Solid Mechanics, Lehigh University, Bethlehem, PA, 1973).
30. J. R. TINGLE, C. A. SHUMAKER, D. P. JONES and R. A. CUTLER, "Chevron-Notched Specimens: Testing and Stress Analysis", ASTM STP 855, edited by J. H. Underwood, S. W. Freiman and F. I. Baratta (American Society for Testing and Materials, Philadelphia, PA, 1984) p. 281.
31. R. A. CUTLER, W. PRECHT and J. A. AUSTIN, Terra Tek Report TR 82-21 (1982).
32. J. TWEED, *Int. J. Eng. Sci.* **8** (1970) 793.

Received 8 July

and accepted 2 November 1984